PUCHAO YANG[1*], JUN WEN[2], XIE WENAN[2],
GANG DAI[2], XIUTING YANG[3]

EXPERIMENTAL INVESTIGATION ON MICROSTRUCTURE EVOLUTION AND CREEP BEHAVIOUR OF RED SANDSTONE AT ELEVATED TEMPERATURE

The changes in the physical and mechanical properties of rocks under high temperatures can impact the construction safety and stability of underground geotechnical engineering. This study focuses on red sandstone treated at different temperatures, employing nuclear magnetic resonance (NMR) spectroscopy to reveal alterations in the internal pore distribution due to elevated temperatures. The results indicate that high temperatures lead to the formation of micro- to meso scale pores and macro-scale pores and cracks. Additionally, high temperatures cause a significant reduction in load-bearing capacity, accompanied by changes in creep behaviour, including a shortened steady-state creep time and an increased strain threshold for rock failure. To more accurately describe the creep behaviour of red sandstone under different temperatures and stress conditions, a novel non-constant creep model is proposed, combining a generalised Kelvin body and a fractional viscoplastic body to demonstrate its versatility in elastic, viscoelastic, and viscoplastic deformation. The model parameters are determined through numerical optimisation, and the model's reliability is confirmed by comparing theoretical curves with experimental data. Sensitivity analysis highlights the critical roles of parameters such as shear modulus, viscosity coefficient, fractional order, and characteristic parameters in capturing various creep patterns, emphasising the model's wide applicability. This research provides profound insights into the physical and mechanical responses of red sandstone to high temperatures and offers valuable information for engineering and geological applications in relevant fields.

Keywords: Temperature treatment; Red sandstone; Creep behaviour; Nuclear magnetic resonance (NMR); Sensitivity analysis

1   XI'AN UNIVERSITY OF SCIENCE AND TECHNOLOGY, XI'AN, SHAANXI PROVINCE, CHINA
2   CHINA COMMUNICATIONS CONSTRUCTION COMPANY LIMITED SECOND HIGHWAY ENGINEERING BUREAU, XI'AN, SHAANXI PROVINCE, CHINA
3   LUAN COAL CHEMICAL GROUP LUNING XINYU COAL INDUSTRY CO., LTD., SHANXI PROVINCE, CHINA

*   Corresponding author: 359163601@qq.com
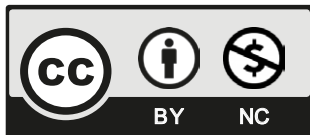
1. Introduction

The influence of high-temperature environments has spurred extensive research and attention within deep subsurface geotechnical engineering. Projects such as in-situ oil shale extraction [1], geothermal energy extraction [2,3], residual coal resource extraction in areas prone to spontaneous combustion [4,5], deep geological disposal of radioactive nuclear waste [6], and the reconstruction of subterranean chambers after fires are all subject to the impact of exceptionally high-temperature conditions [7], posing significant challenges to the stability of surrounding rock and the safety of these engineering endeavours.

Temperature exerts a profound and far-reaching influence on the physical and mechanical attributes of rocks. At the outset, elevated temperatures can trigger interior thermal damage, chemical alterations, and pore pressure shifts in rocks, which can give rise to the propagation of micro-cracks and diminish the strength and stability of the adjacent rock formations. Deng et al. employed acoustic emission (AE) monitoring [8], microscopic observation, and X-ray diffraction (XRD) to investigate the potential damage mechanism associated with temperature's impact on the physical and mechanical properties of granite in geothermal engineering projects, confirming a correlation between mechanical property changes and chemical alterations. Guo et al. conducted uniaxial compression tests on shale specimens that underwent heat treatment at varying temperatures, monitoring their acoustic emissions [9]. When the specimens reached the threshold temperature for macroscopic thermal damage, a "thermal explosion" occurred. The threshold temperature and intensity of this thermal explosion were found to be related to the bedding plane angle. In the context of underground coal conversion and the extraction of residual coal resources in coal spontaneous combustion areas, Zhou et al. introduced a thermal expansion coefficient to construct a directional crack strain constitutive model induced by thermal stress [10].

Additionally, key parameters such as the tensile strength, compressive strength, elastic modulus, and Poisson's ratio of rocks can change high-temperature environments, posing a potential threat to the safety and stability of construction projects. Liu et al. conducted high-temperature conventional triaxial compression tests on shale samples to investigate the relationship between temperature and parameters such as peak strength, elastic modulus, Poisson's ratio, cohesion, and internal friction angle based on experimental results [11]. Tian et al studied the influence of high temperature on the surrounding rock at an in-situ coal conversion site, finding that the permeability, porosity, and compressive strength of the surrounding rock are significantly affected by temperature [12]. This has a significant impact on the stability of gasification coal seam cavities and subsequent carbon storage safety. Yang et al. [13] and Pan et al. [14] proposed the concept of temperature strain rate to describe the relationship between sandstone strain and temperature, utilising acoustic emission technology to monitor real-time sandstone crack evolution in uniaxial compression experiments at varying temperatures while quantitatively analysing the influence of temperature on sample deformation behaviour. An increasing number of researchers are exploring the alterations in physical and mechanical properties of different types of surrounding rocks under high-temperature conditions in diverse engineering geological settings to ensure the reliability and safety of these projects.

Meanwhile, research has also been conducted on the high-temperature creep damage models of different types of rocks. Ren et al. [15] studied the relationship between instantaneous strain, creep strain, and stress in red sandstone samples subjected to high-temperature treatment. They also elaborated on the creep characteristics and strength of the samples under different temperature gradients. Pan et al. [16] discussed the peak strain, uniaxial compressive strength, Young's

modulus, creep strain, and long-term strength of sandstone at different temperatures. They established a nonlinear viscoelastic plastic creep model that can reflect the entire creep process of sandstone under different temperatures. Chen et al. [17] observed a significant influence of temperature on the creep behaviour of granite. Based on this understanding, they combined the process of damage evolution and constructed a creep model that describes the time-dependent behaviour of granite under different temperatures. Chen [18] and his colleagues found that as the heating temperature increases, the peak stress and elastic modulus of heated granite decrease, while the peak strain increases and the fatigue life decreases with increasing temperature. The damage parameter shows a linear relationship with the fatigue life. Zhang et al. [19] used triaxial creep mechanical tests and acoustic emission monitoring methods on shale under different temperatures and confining pressures. They improved the classic Poynting-Thomson creep model to establish an improved creep model that regards temperature and viscoelastic plastic deformation. Rybacki et al. [20] conducted deformation experiments on low-maturity, porous, and carbonate-rich Boreal oil shale using a high-temperature and high-pressure deformation device to estimate the healing rate of water-induced fractures in oil shale reservoirs. They found that the creep rate of oil shale significantly increases under high differential stress, high temperature, and low pressure. Zhou et al. [21] conducted creep experiments at different temperatures and confining pressures based on the high-temperature creep characteristics of gas coal. They introduced a new nonlinear viscoelastic model and constructed a high-temperature creep constitutive model for gas coal.

Nuclear magnetic resonance (NMR) spectroscopy is an effective method for studying the evolution of microscopic pore structures and the micro-mechanisms of creep damage in rocks. Consequently, some researchers have integrated NMR into the study of variations in the pore structures of rocks [22]. In addressing the sensitivity of granite's mechanical properties and pore structure to significant temperature changes in nuclear waste storage environments, Wu et al. [23] investigated the pore structure and mechanical properties of Beishan granite after heat treatment. The study revealed that elevated temperatures significantly influenced the T-2 spectrum distribution, pore size distribution, porosity, compressive strength, and elastic modulus of granite. Furthermore, Pan et al. [24], by considering the changes in pore characteristics during the creep phase and the deformation features of sandstone, explored the creep damage mechanism of sandstone. Additionally, Esmaili et al. [25] conducted a study on eight core samples collected from the South Pars gas field reservoir. Utilising the Magnetic Resonance Imaging Logging (MRIL) method, they identified the PSD changes corresponding to the depth of the entire logging interval.

This research is dedicated to the examination of sandstone subjected to varying temperatures. Graded creep experiments were conducted, and a creep model based on fractional calculus was established. Additionally, nuclear magnetic resonance was employed to unveil alterations in the internal micro-pore structure of sandstone following high-temperature treatment. The primary objective is to enhance our understanding of the influence of elevated temperatures on sandstone.

2. Samples and experimental methods

2.1. Samples

This experiment selected the nearly horizontal Cretaceous Jian'ge Formation (Kjn) sandstone from the Baomiao Tunnel section of the Taoyuan to the Bazhong Expressway in Sichuan Province as the research subject. The sandstone layer belongs to the Chuanbei Tongjiang Sub-basin

in the Sichuan Basin and is primarily formed through a delta-lacustrine deposition. This sandstone exhibits high strength, stiffness, and notable sensitivity to water.

Following the standards set by the International Society for Rock Mechanics (IRSM), large sandstone blocks were fashioned into standard cylindrical specimens of φ50 mm × 100 mm. The specimens were ground using a grinder until the unevenness on both end faces was less than 0.05 mm.

To assess the uniformity of the prepared samples, those exhibiting high uniformity and consistent texture were categorised into six groups (A to F). The fine surface structures of the red sandstone specimens were observed using a Dino-lite electronic microscope, with magnifications of 100 and 200 times (see Fig. 1). The primary components of the red sandstone are quartz, with a localised presence of clay and metallic minerals. The overall porosity of the rock is relatively high, and its connectivity is well-established.
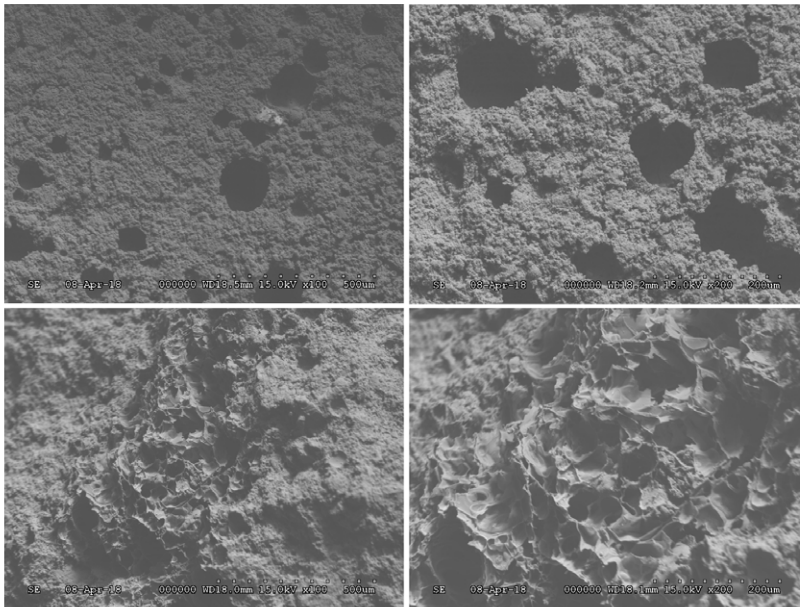

Fig. 1. SEM Images of Red Sandstone Samples (Magnified at 100× and 200×)

2.2. Experimental methods

To investigate the creep characteristics and microstructural changes of sandstone after exposure to high temperatures, nuclear magnetic resonance spectroscopy and multi-level load creep experiments were performed to study the microscopic pore structure and creep characteristics of sandstone cooled after exposure to different high temperatures.

Nuclear Magnetic Resonance (NMR) Spectroscopy: When a substance containing magnetic nuclei is immersed in a magnetic field, nuclear magnetic resonance relaxation can be excited. The surface relaxation time of rock particles can approximate the transverse relaxation time of porous media. Surface relaxation often occurs at the fluid-solid interface and is closely related

to the pore structure of porous media [26]. The relationship between surface relaxation time and pore radius can be characterised using Equation (1):

$$\frac{1}{T_{2S}} = \rho \left(\frac{S}{V} \right)_{pore} = \frac{c}{r} \tag{1}$$

In the equation, T_{2S} represents the surface relaxation time in milliseconds (ms), is the particle surface relaxation rate, r is the pore radius in micrometres (µm), and c is a dimensionless parameter associated with the pore. According to Equation (1), the transverse relaxation time obtained from nuclear magnetic resonance curves can be used to approximate the pore size of porous media.

Testing Procedure: The rock cores, subjected to various temperature treatments, were evacuated for 4 hours and saturated with formation water under a pressure of 30 MPa for 72 hours. Subsequently, the standard samples were placed into the rock core holder, and the T_2 spectra of the rock samples at different temperatures were measured using a nuclear magnetic resonance instrument. The Nuclear Magnetic Resonance (NMR) spectrometer was the Bruker Avance III from Switzerland, operating at a magnetic field strength of 18.7 Tesla. The radiofrequency (RF) pulse frequency ranged from 1 to 30 MHz, with an RF frequency control accuracy of 0.1 Hz. The coil diameter of the probe was 25 mm, able to conduct NMR T2 spectrum tests for small-diameter rock cores with a minimum length of 25 mm.

Multi-level load creep experiments: To investigate the effect of temperature on the rheological behaviour of red sandstone, multi-level load creep experiments were conducted on the red sandstones subjected to different high temperatures [27]. Twelve standard cylindrical red sandstone rock samples (φ50×100) that conform to the ISRM recommendation were prepared for the experiments [28]. Fig. 2 illustrates the schematic diagram of the furnace and triaxial testing machine used for the experiments. Initially, the samples were categorised into six distinct groups,
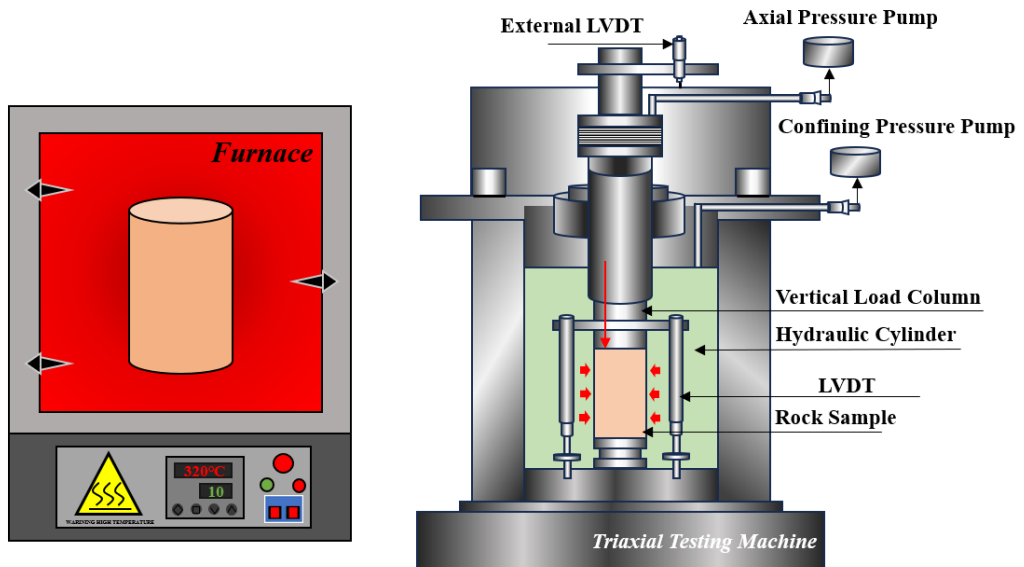

Fig. 2. Diagram of experimental instruments

with each group aligned with a specific temperature condition: ambient temperature (30°C), 80°C, 140°C, 200°C, 260°C and 320°C, respectively. To minimise the potential for experimental variables, two samples were tested in the same conditions.

Subsequently, each group sample was sequentially put into a furnace and subjected to the uniform heat treatment for a rate of 10°C/min to reach the specified temperature after being thermally treated for two hours, the samples were removed from the furnace and allowed to cool naturally.

Once fully cooled, the samples were then transferred to a triaxial servo-controlled testing machine for creep experiments, and then the following operation process can be divided into three steps: (a) the sample after thermal treatment was positioned on the axial load table, slowly lowered the hydraulic cylinder until the chamber can be holistically sealed, and slowly lowered the vertical load column to make contact with the sample; (b) the axial pressure pump was activated to apply axial stress of 1 MPa to guarantee the sample was pre-tightened. Flowing this, turn on the confining pressure pump to apply a confining pressure of 10 MPa; (3) Since 75% of red sandstone's compressive strength was categorised into seven load levels, the load increment for multi-level load creep experiment was set to 30 MPa, with load duration of 48 hours. The axial deformation of red sandstone was precisely measured by a pair of LVDT sensors mounted on the vertical load column, and the ultimate axial strain of sandstone was calculated by selecting the average value from the sensors.

3. Experimental results and analysis

3.1. Nuclear magnetic resonance spectrum analysis

The porosity varies across different rock types, resulting in distinct positions and quantities of hydrogen atoms reflected in nuclear magnetic resonance (NMR) signals. Consequently, utilising the NMR signals from hydrogen atoms enables the tracking of the initiation and propagation of fractures in rock samples under varying conditions. Within the rock pores, three distinct relaxation mechanisms are present, encompassing free relaxation, surface relaxation, and diffusion relaxation. Their corresponding T_2 relaxation times can be expressed as follows:

$$\frac{1}{T_2} = \frac{1}{T_{2b}} + \frac{1}{T_{2s}} + \frac{1}{T_{2d}}$$ (2)

Here, T_{2b} signifies the transverse relaxation time originating from the free state, T_{2s} represents the transverse relaxation time of signals induced by surface relaxation, and T_{2d} indicates the lateral relaxation time of signals caused by diffusion relaxation under a gradient magnetic field. As indicated by Equation (1), it is evident that in saturated samples, surface relaxation plays a pivotal role, with T_2 being directly proportional to the pore size. The NMR-T_2 distributions of sandstone samples, subjected to different temperature treatments (20°C, 80°C, 140°C, 200°C, 260°C, and 320°C), are illustrated in Fig. 3.

Fig. 3 depicts the changes in the T_2 spectrum distribution of red sandstone before and after high-temperature treatments in the range of 20°C to 320°C. According to the principles of rock nuclear magnetic resonance, the magnitude of the transverse relaxation time (T_2 value) is positively correlated with the pore size where the measured fluid is located. Following the approach of H. Jia et al. [29,30], considering the relaxation characteristics of fluids in different
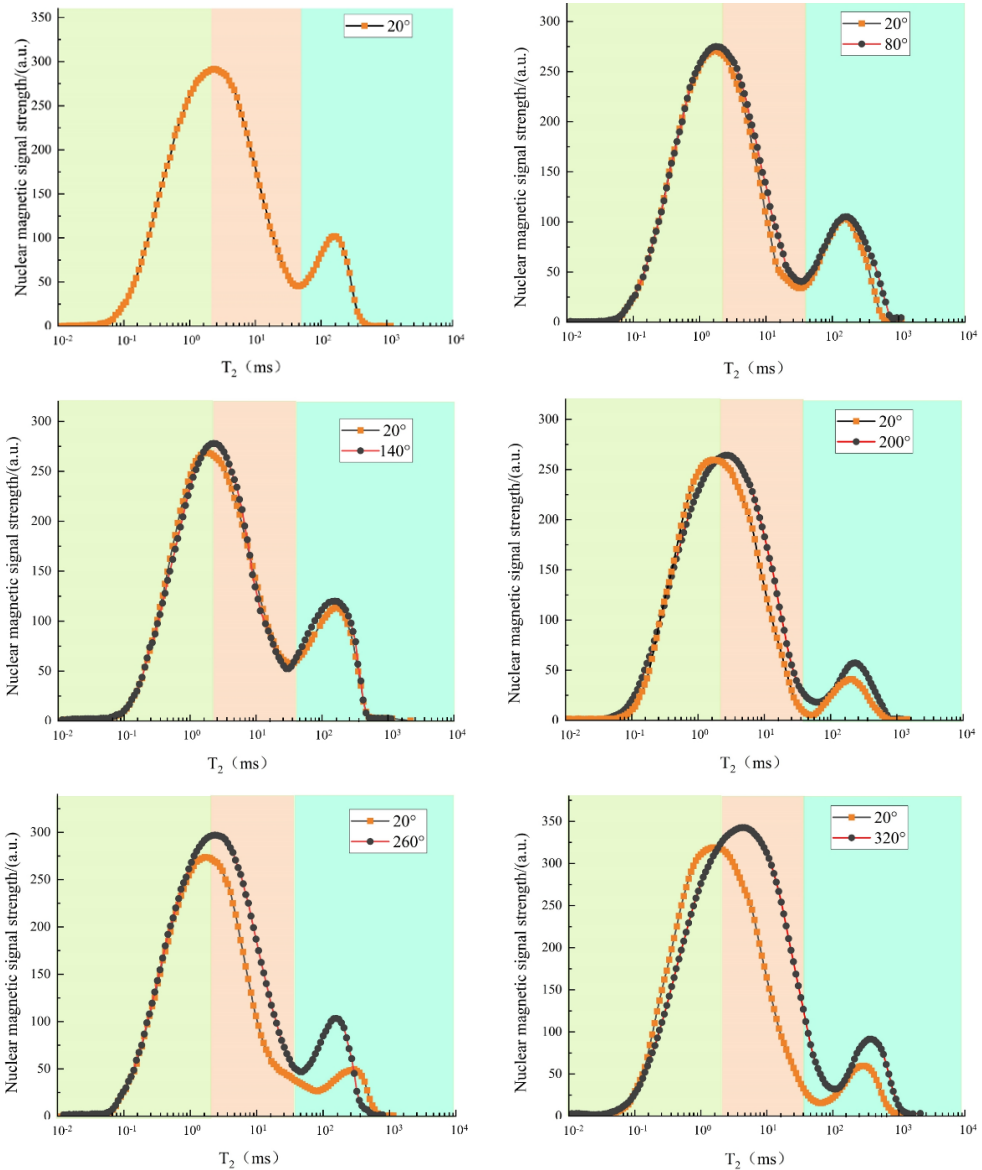
Fig. 3. T_2 Spectrum of Red Sandstone after Different Temperature Treatments

pores, sandstone pores can be categorised into three types: pores corresponding to $T_2 < 3$ ms are termed micropores, those with T_2 values in the range of 3 to 33 ms are referred to as mesopores, and pores corresponding to $T_2 > 33$ ms are categorised as macropores.

In Fig. 3(a), the nuclear magnetic resonance (NMR) saturation T_2 spectrum of sandstone at 20°C exhibits a bimodal distribution. Through spectral peak morphology analysis, it is evident that the peak corresponding to micro-mesopores (P1) is prominent, followed by the macropore

peak (P2). This indicates an uneven distribution of internal pore and fracture networks in the sandstone, with well-developed micro-mesopores but underdeveloped macropores and fractures. The proportions of the areas under the two peaks are 87.8% and 12.2%, respectively. The lack of clear boundaries between the two peaks and good continuity suggests effective interconnectivity between pores and fractures.

During the temperature treatment stage from 80°C to 200°C, the amplitude of the P1 peak shows an increasing trend compared to the low-temperature stage, as shown in Fig. 3(b-d). However, the overall proportion of P1 remains around 80%, indicating that micro-sized pores dominate the pore size distribution during this stage. With an increase in temperature, the peak amplitude of P1 increases and shifts to the right, suggesting that the temperature effect leads to an increase in the content of micro-mesopores and macropores-fractures, resulting in an overall increase in average pore size. However, the interconnectivity between these features remains largely unchanged.

In the temperature range of 200°C to 320°C, as depicted in Fig. 3(d-f), the amplitude of the P1 peak increases after high-temperature treatment. When the temperature exceeds 260°C, the distribution range of the T_2 spectrum peaks widens, indicating an expansion in the range of pore sizes. The amplitudes of P2 and P3 peaks significantly increase, shifting towards larger T_2 values, indicating the formation of more micro-mesopores and macropores-fractures. Both P1 and P2 peaks exhibit a rightward shift, suggesting an increase in average pore size based on the pore size distribution characteristics. These results are attributed to the high temperature causing physical and chemical reactions in the mineral components of the sandstone, leading to changes in internal pore and fracture distribution and connectivity. The elevated temperature promotes the increase of micro-mesopores and macropores-fractures.

3.2. The impact of temperature on pore structure

To quantitatively articulate the influence of temperature on pore size distribution, pore distribution charts for the samples under different temperature treatments were constructed based on the T_2 spectrum.

Due to the varying initial pore size distributions among different samples, a normalisation process was employed to better illustrate the impact of temperature on the pore size distribution of red sandstone. The increments in the proportions of different pore sizes before and after each temperature treatment were calculated. As depicted in Fig. 4, for the same sample, there is an overall gradual reduction in the content of micro-pores after high-temperature treatment. Specifically, as the temperature increases from 20°C to 800°C, the proportion decreases from 93.5% to 88%. Conversely, the content of macropores exhibits an overall increase with rising temperature. As the temperature increases from 20°C to 320°C, the proportion increases from 6.5% to 12%.

In summary, the pore size distribution of sandstone after different temperature treatments, as revealed by nuclear magnetic resonance testing, exhibits a bimodal distribution. Comparative analysis of the changes in pore size distribution after different temperature treatments indicates that the elevation in temperature induces the development of micro-sized pores, transforming them into larger-sized pores. This phenomenon leads to an overall increase in the porosity of the sandstone. The continuous increase in porosity reflects the internal structural damage caused by high-temperature treatment, resulting in the generation of new pores and improving the permeability characteristics of the sandstone.
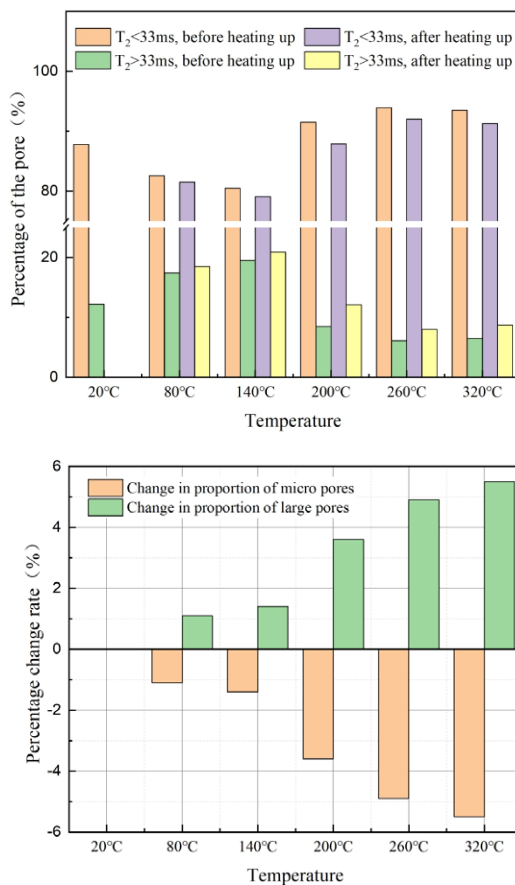
Fig. 4. Pore size distribution of samples before and after high-temperature treatment
at different temperatures

Due to the continuous evaporation of various moisture and changes in mineral composition inside the sandstone caused by high temperatures, coupled with numerous physical and chemical reactions, the original pore structure within the sandstone is severely disrupted. This disruption results in the creation of numerous new pore structures, leading to an increase in porosity. The porosity of sandstone samples treated at different temperatures varies with the temperature change. Fig. 6 illustrates the variation pattern of porosity increments in sandstone samples treated at different temperatures.

From Fig. 6, it is observed that the porosity of the sandstone increases linearly with the temperature rise, resulting in a linear increase in the porosity increment values. As the temperature increases, high-temperature behaviour promotes the initiation of new micro-cracks in the sample, leading to an increase in porosity. When the temperature exceeds 200°C, a significant number of micro-cracks extend, coalesce, and form macroscopic cracks, resulting in a rapid increase in porosity. Zhou et al. [31] also suggest that the initiation, extension, and coalescence of micro-cracks during the creep stage are the main reasons for the increase in porosity. They propose that
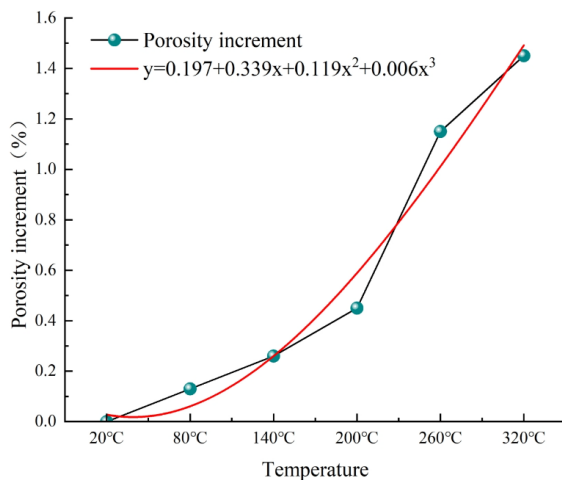
Fig. 6. Porosity Increment at Different Temperatures

the increase in temperature stress promotes the initiation of micro-cracks in the rock, leading to an increase in rock porosity. Additionally, from Fig. 6, it is observed that the slope of the curve increases first and then decreases with the increase in temperature. This indicates that within a certain range, higher temperatures have a more significant impact on the porosity increment values in response to temperature-induced strain.

The microstructural characteristics of rocks under high-temperature conditions are relevant to various fields, including geotechnical engineering, mining, geology, and energy. The development and utilisation of underground spaces, the extraction of deep-seated mineral resources, and the exploitation of geothermal resources all face changes in the mechanical properties of rocks under high-temperature environments. Therefore, studying the variation patterns of rock porosity under high-temperature conditions is of great significance. Using nuclear magnetic resonance technology, this study analysed the impact of high temperatures on the porosity and pore structure of sandstone. The results indicate that, under conditions ranging from 20°C to 320°C, the relationship between temperature and the increment of porosity roughly conforms to a cubic function. Through quantitative analysis of nuclear magnetic resonance parameters, the distribution of porosity in sandstone under different temperature conditions was discussed. Before 200°C, the main manifestation involves the shrinkage of clay minerals, and the evaporation of water, leading to the further opening of primary fractures, while the secondary fractures remain relatively scarce. From 200°C to 320°C, extensive drying cracks (desiccation cracks) in clay minerals generate new fine cracks. Simultaneously, the anisotropic thermal expansion forces between mineral grains lead to the opening of fractures at the boundaries between mineral crystals and clay minerals, which results in a significant increase in both porosity and permeability.

3.3. Effect of temperature on creep behaviour of red sandstone

Fig. 7 shows the creep curves of red sandstone samples subjected to various thermal treatments, an evident observation from the figure is that the load capacity of red sandstone decreases

with increasing temperature, especially when temperature is above 140°C. The entire deformation process of red sandstone consists of four stages: instantaneous deformation, attenuation creep, stable creep, and accelerated creep [32]. The instantaneous deformation constitutes the majority of total deformation and its increment initially decreases then increases with increasing load level. Specifically, the strain increments of red sandstone subjected to 80°C thermal treatment are 0.19%, 0.16%, 0.16%, 0.22%, 0.23% and 0.25%, respectively, which indicates the general phenomenon of crack compaction, elastic period and crack propagation. Creep deformation, on the other hand, is relatively small, which has a direct proportion with the load level, and follows the mechanical behaviour of hard rock [33].

Notably, in the same load level the higher the temperature is, the greater the total deformation gets, and there is a sharp rise of deformation between 140°C and 200°C, which means when the temperature exceeds 140°C the thermal damage of red sandstone gets strong. In addition, the accelerated creep damage of red sandstone is observed after 140°C, 200°C and 260°C thermal treatment, and under the ultimate stress level the stable creep duration decreases with the increase of temperature, which implies the high temperature not only contributes to rock deterioration but enhances its brittle response.
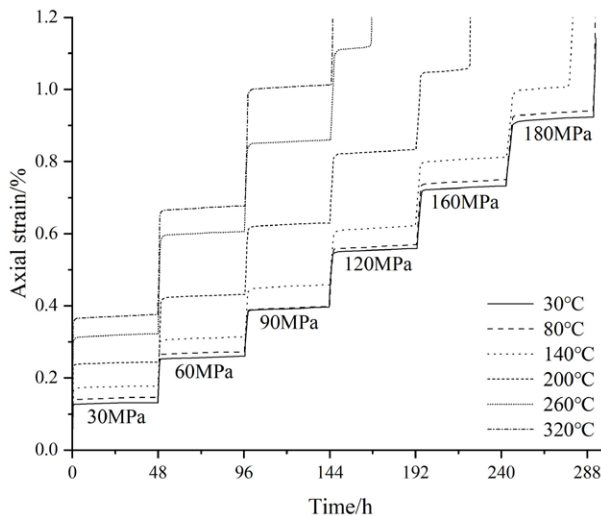

Fig. 7. Creep curves of red sandstone after different temperature treatment

Fig. 8 shows the relationship between the average stable creep rate and deviatoric stress. The relationship approximately follows the parabolic law, substantially the creep rate has a sluggish growth, and only under the ultimate stress appeared a sharp growth. Coherently, the higher the temperature is, the greater the creep rate gets. Given these observations, the steady-rate tangent method is deemed appropriate for determining the long-term strength of red sandstone [34,35], which is a vital parameter for assessing the long-term stability of geological formations, as shown in Fig. 9. The fitting curves of the relationship between the average stable creep rate and deviatoric stress are obtained by the least square method, exhibiting an exponential growth pattern. The intersection point of the oblique asymptote of the fitting curves is determined as

the long-term strength, consequently, it can be seen that the long-term strength decreases with the increase of temperature, and the strength loss becomes more obvious after 200°C thermal treatment.
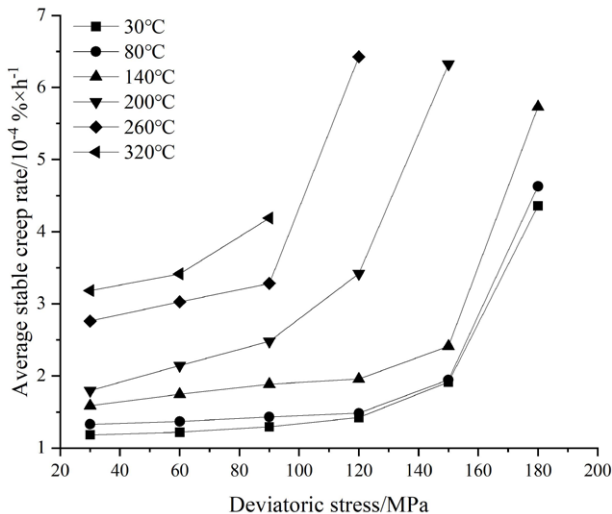

Fig. 8. Average stable creep rate vs. deviatoric stress of red sandstone after different temperature treatment
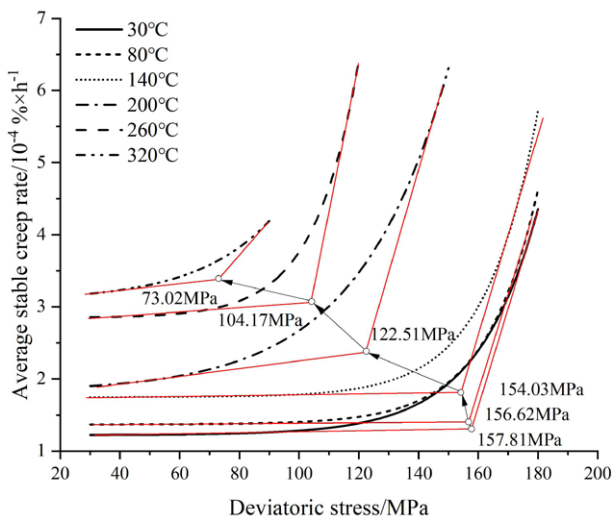

Fig. 9. Long-term strength of red sandstone determined by steady-rate tangent method

The red sandstone failure mode with different temperature treatments is shown in Fig. 10. Notably, all samples exhibit a shear failure pattern, with a primary oblique shear crack consistently

propagating from the top to the bottom of the samples, this primary crack is often accompanied by multiple secondary shear cracks.

The temperature below 200°C appears to have minimal influence on the failure mode of red sandstone. However, when the temperature exceeds 260°C, the secondary cracks in the sample start to connect with the main crack, creating a larger shear failure surface. This effect becomes particularly obvious after 320°C thermal treatment, resulting in a penetrating shear failure, and rock fractured more severely.

(a) 30°C　　　(b) 80°C　　　(c) 140°C　　　(d) 200°C　　　(e) 260°C　　　(f) 320°C
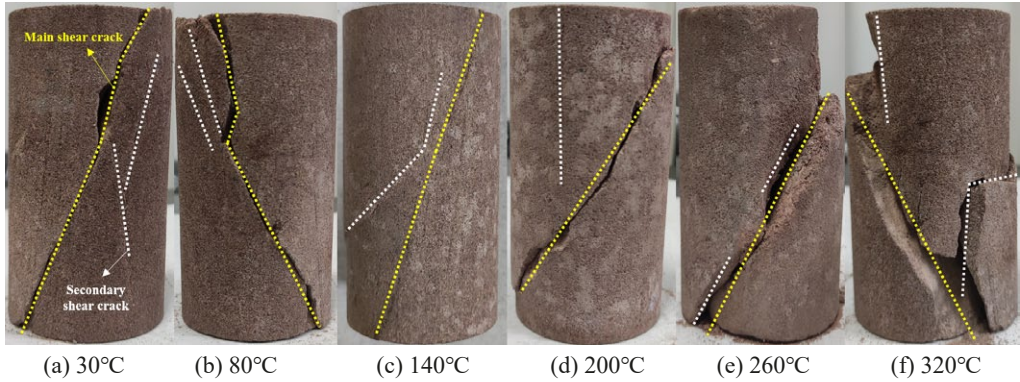
Fig. 10. Failure mode of red sandstone after long-term loading

4. Discussion

4.1. Non-stationary creep model considering thermal damage

To precisely describe the creep behaviour of red sandstone after different temperature treatments, we proposed a creep model which consists of a general kelvin body and a fractional visco-plastic body connected in series, as shown in Fig. 11. The general kelvin body can simulate

Fig. 11. Diagrammatic sketch of creep model

the non-failure creep behaviour, including the instantaneous deformation, attenuation creep and stable creep, its constitutive equation can be expressed as [36]:
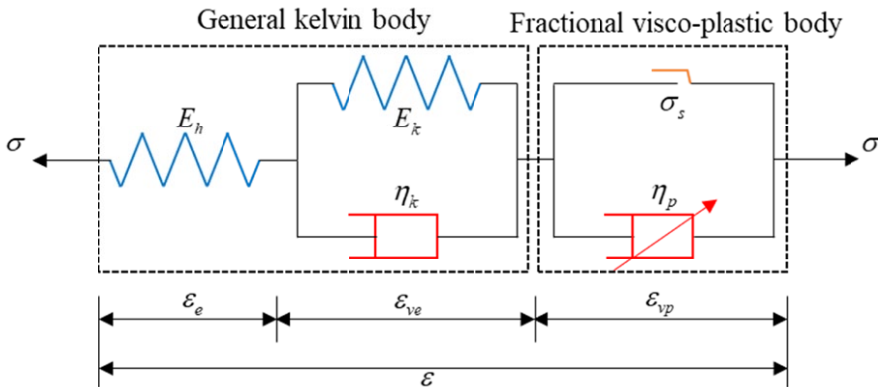
$$\varepsilon_e + \varepsilon_{ve} = \frac{\sigma}{E_h} + \frac{\sigma}{E_k}\left[1 - \exp\left(-\frac{E_k}{\eta_k}t\right)\right] \tag{3}$$

where σ is the total stress; ε_e and ε_{ve} represent the strain of elasticity and viscoelasticity; E_h and E_k represent the elastic modulus of first and second spring from left to right; η_k is the viscosity coefficient; t is the creep time.

The visco-plastic body takes effect by in parallel connecting a switch and non-newtonian dashpot, the switch dictates whether the body works by introducing a yield criterion. The non-newtonian dashpot can reflect the mechanical performance between the ideal solid and fluid, its constitutive equation can be described as follow:

$$\sigma = \eta_p \frac{d^\mu \varepsilon_{vp}}{dt^\mu} \tag{4}$$

where η_p is the viscosity coefficient of non-newtonian dashpot; μ is the factional order which can be an arbitrary real or complex number [37]. Eq. (4) can be solved by the Riemann-Liouville fractional-order integral operator, let $f(t)$ be integrable when $t \in (0,\infty)$, and $\mathrm{Re}(\mu) > 0$, the R-L fractional integral $_0D_t^{-\mu}$ of continuous function $f(t)$ is:

$$_0D_t^{-\mu}f(t) = \frac{1}{\Gamma(\mu)}\int_0^t (t-\xi)^{\mu-1} f(\xi)d\xi \tag{5}$$

Accordingly, the solution of Eq. (4) is as follow:

$$\varepsilon_{vp} = {}_0D_t^{-\mu}\frac{\sigma}{\eta_p} = \frac{\sigma}{\Gamma(\mu)\eta_p}\int_0^t (t-\xi)^{\mu-1} d\xi = \frac{\sigma t^\mu}{\Gamma(\mu+1)\eta_p} \tag{6}$$

Under the ultimate stress level, the micro-cracks that have accumulated over time gradually propagate and intersect, creating a significant shear failure surface. This process is usually accompanied by a non-linear trend in creep deformation. due to the decreasing capacity area of rock affected by accumulated cracks, the apparent stress calculated by the ratio of applied force to section area of cylinder rock becomes inadequate to represent the real stress, therefore, it is necessary to introduce the concept of effective stress based on the damage mechanic:

$$\sigma' = \sigma(1 - D) \tag{7}$$

where σ' is the effective stress; D is the damage variable.

Assume that the creep time is the continuous random variable of exponential distribution, i.e., $t \sim \exp(\lambda)$, then the damage variable is the cumulative distribution function of one, which can be written as:

$$D = 1 - e^{-\lambda t} \tag{8}$$

where λ is a character parameter of controlling the deformation magnitude during the accelerated creep stage, by substituting Eq. (8) into Eq. (7) the expression of effective stress is got:

$$\sigma' = \sigma \exp(\lambda t) \qquad (9)$$

Furthermore, substitute Eq. (9) into Eq. (4), the non-newtonian dashpot with damage is set as:

$$\frac{d^{\mu}\varepsilon_{vp}}{dt^{\mu}} = \frac{\sigma}{\eta_p}\exp(\lambda t) \qquad (10)$$

Eq. (10) can be solved by introducing the Riemann-Liouville fractional-order integral operator:

$$\varepsilon_{vp} = {}_0D_t^{-\mu}\frac{\sigma\exp(\lambda t)}{\eta_p} \qquad (11)$$

because there is a continuous m-th-order derivative of integrand, Eq. (11) is rewritten by introducing the distribution integral method as:

$$\begin{aligned}
{}_0D_t^{-\mu}\frac{\sigma\exp(\lambda t)}{\eta_p} = \\
= \frac{\sigma}{\eta_p}\left[\sum_{k=0}^{m}\frac{\lambda^k t^{\mu+k}}{\Gamma(\mu+k+1)} + \frac{1}{\Gamma(\mu+m+1)}\int_0^t (t-\tau)^{\mu+m}\lambda^{m+1}d\tau\right]
\end{aligned} \qquad (12)$$

where $\Gamma(x)$ is the gamma function. Actually, when there is an infinite derivative of integrand, Eq. (12) can be extended to an infinite series as:

$$_0D_t^{-\mu}\frac{\sigma\exp(\lambda t)}{\eta_p} = \frac{\sigma t^{\mu}}{\eta_p}\lim_{m\to\infty}\sum_{k=0}^{m}\frac{(\lambda t)^k}{\Gamma(\mu+k+1)} = \frac{\sigma t^{\mu}}{\eta_p}E_{1,1+\mu}(\lambda t) \qquad (13)$$

where $E_{\alpha,\beta}(z)$ is the Mittag-Leffler function.

In order to simplify the equation for subsequent operation, the lower incomplete gamma function is introduced which has the definition as:

$$Igamma(\lambda t, \mu) = \frac{1}{\Gamma(\mu)}\int_0^{\lambda t}\tau^{\mu-1}\exp(-\tau)d\tau \qquad (14)$$

Substitute Eq. (14) into Eq. (13), the optimal expression of visco-plastic deformation is as follow:

$$\begin{aligned}
E_{1,1+\mu}(\lambda t) = \\
= \frac{\exp(\lambda t)(\lambda t)^{-\mu}}{\Gamma(\mu)}\int_0^{\lambda t}x^{\mu-1}e^{-x}dx = \exp(\lambda t)(\lambda t)^{-\mu}\,Igamma(\lambda t, \mu)
\end{aligned} \qquad (15)$$

$$\varepsilon_{vp} = \frac{\sigma t^{\mu}}{\eta_p}E_{1,1+\mu}(\lambda t) = \frac{\sigma\exp(\lambda t)(\lambda)^{-\mu}}{\eta_p}\,Igamma(\lambda t, \mu) \qquad (16)$$

Because the experimental condition above is in a triaxial compression state, the creep model should be generalised to a three-dimensional form. According to the Hooke's law, the constitutive model of the elastic body is as follows:

$$\varepsilon_{ij}^e = \frac{S_{ij}}{2G_m} + \frac{\sigma_m \delta_{ij}}{3K} \tag{17}$$

where ε_{ij}^e is the elastic strain tensor; S_{ij} is the deviatoric stress tensor; σ_m is the spherical stress tensor; δ_{ij} is the Kronecker delta; G_m is the shear modulus; K is the bulk modulus.

It is universally recognized that the creep deformation is activated by the deviatoric stress, in other words, there is no creep phenomenon in the hydrostatic stress field, therefore, the visco-elastic strain can be expressed as:

$$\varepsilon_{ij}^{ve} = \frac{S_{ij}}{2G_k}\left[1 - \exp\left(-\frac{G_k}{\eta_k}t\right)\right] \tag{18}$$

where G_k and η_k represent the shear modulus and viscosity coefficient. In terms of the theory of plasticity, the visco-plastic strain can be expressed as:

$$\varepsilon_{ij}^{vp} = \frac{\exp(\lambda t)}{\lambda^\mu \eta_p}\left\langle \varphi\left(\frac{F}{F_0}\right)\right\rangle \frac{\partial Q}{\partial \sigma_{ij}} Igamma(\lambda t, \mu) \tag{19}$$

where F_0 is the yield function of rock; F_0 is the yield reference; Q is the plastic potential function; $\langle \rangle$ is the yield criterion:

$$\left\langle \varphi\left(\frac{F}{F_0}\right)\right\rangle = \begin{cases} \varphi\left(\frac{F}{F_0}\right) & F \geq 1 \\ 0 & F < 0 \end{cases} \tag{20}$$

φ is a power function. The Von Mises yield criterion and associated flow theory are adopted, and F_0 and power exponent are simplified to 1, then in principle stress space we have:

$$\varepsilon_{ij}^{vp} = \frac{(\sigma_1 - \sigma_3 - \sigma_s)\exp(\lambda t)}{3\lambda^\mu \eta_p} Igamma(\lambda t, \mu) \tag{21}$$

where σ_1 and σ_3 are the maximum and minimum principal stress, σ_s represents the failure stress level. Accordingly, a particular solution of the general Kelvin body and fractional visco-plastic body gets explicit, the total axial strain can be calculated by adding up the strain of these bodies:

$$\varepsilon_{11} = \begin{cases} \dfrac{\sigma_1 - \sigma_3}{3G_m} + \dfrac{\sigma_1 + 2\sigma_3}{9K} + \dfrac{\sigma_1 - \sigma_3}{3G_k}\left[1 - \exp\left(-\dfrac{G_k}{\eta_k}t\right)\right] & \sigma_1 - \sigma_3 < \sigma_s \\[3ex] \dfrac{\sigma_1 - \sigma_3}{3G_m} + \dfrac{\sigma_1 + 2\sigma_3}{9K} + \dfrac{\sigma_1 - \sigma_3}{3G_k}\left[1 - \exp\left(-\dfrac{G_k}{\eta_k}t\right)\right] + \\[3ex] \dfrac{(\sigma_1 - \sigma_3 - \sigma_s)\exp(\lambda t)}{3\lambda^\mu \eta_p} Igamma(\lambda t, \mu) & \sigma_1 - \sigma_3 \geq \sigma_s \end{cases} \tag{22}$$

4.2. Validation and parametric analysis of model

To verify the correctness and reliability of the proposed model, combined with experimental data above each parameter of the model was identified. Based on the numerical optimization and simulation platform of 1stOpt software [38], the universal global optimization algorithm was adopted to realise the parametric estimation and solution for the non-linear complex model; the corresponding model parameters to the experimental data are listed in TABLE 1 and TABLE 2. Below the yield surface rock creep primarily exhibits elastic and viscous deformation characteristics, as seen in TABLE 1, at the same temperature every parameter is positively correlated with the stress level, consistent with common creep experimental results. Contrarily, at the same stress, every parameter is negatively correlated with temperature. To quantify the damage degree affected by the stress level and temperature, a thermal damage variable can be established by extending a fundamental concept of damage mechanics. When the volumetric behaviour is ignored during rock creep, the creep compliance $J(t)$ of the general kelvin body can be written as:

$$\varepsilon_{11} = \frac{\sigma_1 - \sigma_3}{3G_m} + \frac{\sigma_1 - \sigma_3}{3G_k}\left[1 - \exp\left(-\frac{G_k}{\eta_k}t\right)\right] =$$
$$= (\sigma_1 - \sigma_3)\left[\frac{1}{3G_m} + \frac{1}{3G_k}\left(1 - \exp\left(-\frac{G_k}{\eta_k}t\right)\right)\right] = (\sigma_1 - \sigma_3)J(t) \qquad (23)$$

Like the definition of damage variable by the effective elastic modulus, the thermal damage variable during rock creep can be defined as:

$$D = 1 - \frac{1/J^*(t,T)}{1/J(t,T)} = 1 - \frac{J(t,T)}{J^*(t,T)} \qquad (24)$$

where $J^*(t,T)$ is effective creep compliance relevant to time and temperature, subsequently, in unit time the thermal damage variable can be determined by substituting the parameters in TABLE 1. Fig. 12 shows the variation trend of the thermal damage variable with temperature, the inclined S-shaped curves of the thermal damage variable suggest a rapid developing period of thermal damage degree over 140°C, which keeps coherent with the experimental results. Additionally, below 200°C relatively the greater the deviatoric stress, the lower the thermal damage variable, while when the temperature is higher than 200°C, the variables are almost the same.

TABLE 1

Identification parameters of creep model below yield surface

Stress/MPa	Temperature/°C	G_m/GPa	K/GPa	G_k/GPa	η_k/GPa×h
1	2	3	4	5	6
30	30	36.34	48.45	7.69	2.56
	80	34.47	45.96	6.97	2.13
	140	27.96	37.28	5.78	2.11
	200	22.66	30.22	4.15	1.41
	260	19.65	26.20	3.39	1.01
	320	15.83	21.10	2.90	0.83

TABLE 1. Continued

| 1	2	3	4	5	6
60	30	16.45	21.94	22.29	9.54
	80	15.87	21.16	20.55	9.70
	140	12.26	16.34	23.46	9.47
	200	9.93	13.24	13.33	7.18
	260	7.65	10.20	8.24	5.30
	320	6.57	8.75	7.89	3.92
90	30	13.61	18.15	30.26	26.09
	80	13.75	18.33	28.72	26.03
	140	12.15	16.19	24.04	21.24
	200	8.32	11.09	20.81	13.08
	260	6.28	8.38	13.63	10.68
	320	5.80	7.74	9.32	8.36
120	30	12.15	16.20	32.36	35.03
	80	12.44	16.59	27.71	29.12
	140	11.09	14.79	27.90	32.46
	200	8.00	10.66	23.21	24.20
150	30	11.34	15.11	31.94	41.24
	80	10.74	14.32	35.45	41.02
	140	10.19	13.58	29.55	41.18
180	30	10.22	13.62	37.04	70.43
	80	9.87	13.16	39.40	66.00
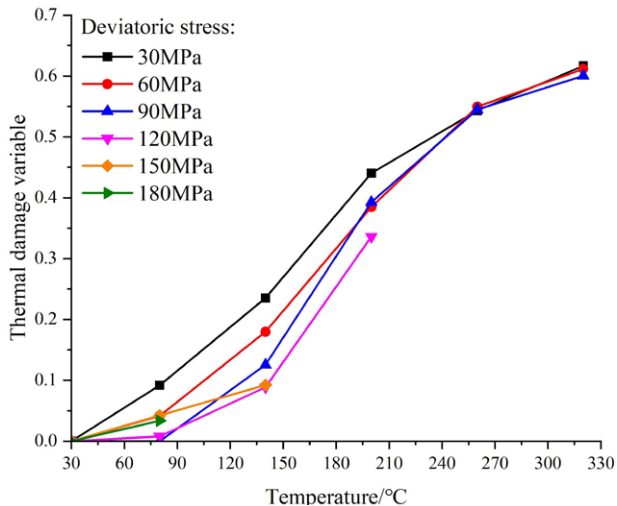
Fig. 12. Thermal damage variable vs. temperature of red sandstone under different stress levels

Although there is a positive correlation between the stress and damage variable, it is important to perceive that the effect of temperature on creep damage is much stronger than the stress,

which is evident from the provided example, where the maximum range of damage variable only reaches 0.15 at constant temperature (140°C), while it can range within 0.6 under constant stress (30 MPa, 60 MPa and 90 MPa). Consequently, to a considerable degree, the temperature governs the creep amplitude of red sandstone before failure stress.

All of the identified parameters of the creep model to the red sandstone experienced accelerated creep are given in TABLE 2. The elastic and visco-elastic parameters have an identical decreasing pattern with increasing temperature. However, the visco-plastic η_p and character parameter λ exhibit a slight increasing trend. The fractional order μ remains relatively constant below 200°C but significantly decreases at 260°C.

TABLE 2

Identification parameters of creep model on yield surface

Stress/MPa	Temperature/°C	G_m/GPa	K/GPa	G_k/GPa	η_k/GPa×h	η_p/GPa×h$^\mu$	μ	λ
180	140	9.75	13.00	28.45	60.90	6.15	103.16	4.01
160	200	8.60	11.47	21.18	33.57	9.61	102.39	6.08
120	260	6.34	8.45	13.76	19.26	10.39	78.57	6.25

From a superficial perspective, the decrease in elastic and visco-elastic parameters with increasing temperature may be due to the softening effect of temperature on the material. As the temperature rises, the internal structure of the material becomes more disordered, which improves the creep performance of red sandstone. The variation in fractional order μ and character parameter λ with temperature may be attributed to the activation of creep mechanisms such as dislocation glide and grain braking at higher temperatures, which significantly promotes the occurrence of accelerated creep in advance.
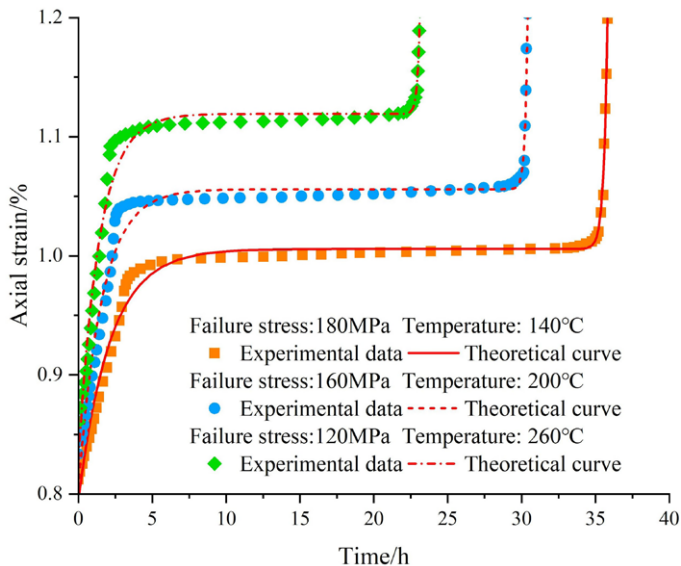

Fig. 13. Comparison of experimental data and theoretical curve of creep model under failure stress level

Substitute the identified parameters into Eq. (22), and the corresponding theoretical curves to the experimental data can be obtained as seen in Fig. 13. It can be revealed from the figure the high coincidences between the curve and data demonstrate the correctness and reliability of the model.

Simultaneously, the following conclusions can be drawn from the data under ultimate stress level, a higher temperature results in (1) a lower stress to trigger the accelerated creep; (2) a shorter duration of stable creep; and (3) a larger strain threshold to rock failure. To discuss how the creep model represents these features, the sensitivity analysis of the parameters of the model was performed as shown in Fig. 14, the theoretical curve of the sample subjected to 260°C thermal treatment and 120MPa deviatoric stress was set as a baseline, the control variable method was adopted to study how some of the critical parameters manipulate the shape of the curve. Only respectively adjusting the shear modulus Gk from 13.76 GPa to 18 GPa, 22 GPa, 26 GPa and 30 GPa, a series of family curves marked with a solid line can be obtained, which shows that the shear modulus Gk primarily determines the total strain before entering accelerated creep failure. The smaller the shear modulus Gk, the larger the strain. Similarly, by adjusting the viscosity co-efficient ηk from 19.26 GPa×h to 25 GPa×h, 31 GPa×h, 37 GPa×h and 42 GPa×h respectively, it is apparent to recognize that the viscosity coefficient can regulate when the attenuation creep comes to an end, in other words, the greater the viscosity coefficient, the longer the duration of attenuation creep. The introduction of a fractional visco-plastic body effectively compensates for the disadvantage of the conventional visco-plastic body being incapable of describing the non-linear mechanical behaviour in tertiary creep, where fractional order regulates when the stable creep comes to an end corresponding to the start-up time to accelerated creep, the smaller the fractional order, the faster the rock failure.

In addition, from the mathematical quality of the model itself, the character parameter λ has the same equivalent role of coordinating the start-up time in tertiary creep, because λ is constantly multiplied by time, and it is convenient to extrapolate that the viscosity coefficient η_p regulates
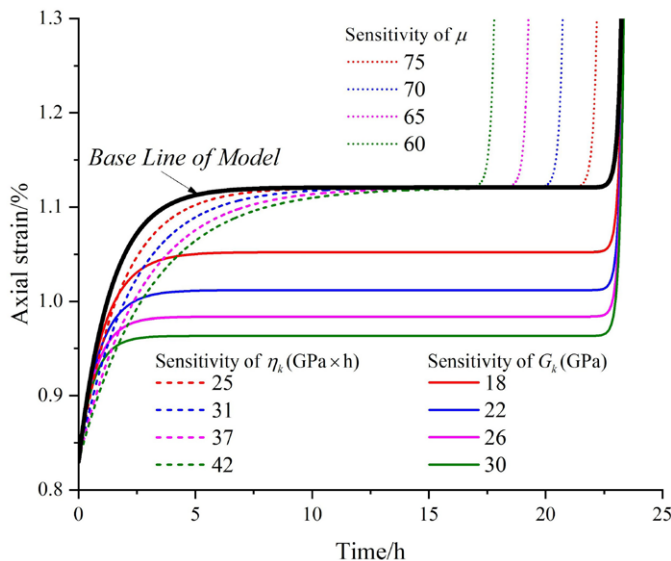

Fig. 14. Sensitivity of key parameters of creep model

the creep rate in tertiary creep. Consequently, changing these parameters can essentially meet all various kinds of creep patterns, which reflects the broader applicability and serviceability of the model.

5. Conclusion

1. With increasing temperature, the pore structure of red sandstone undergoes significant changes, characterised by an increase in micro-mesopores and the formation of macropores-fractures. The elevated temperature leads to water evaporation and mineral composition changes, disrupting the original pore structure and significantly increasing the rock's porosity. This change in pore structure impacts the rock's permeability and permeation properties, which is significant for geological engineering, mining, and energy exploration.

2. The creep behaviour of red sandstone is categorised into four stages: instantaneous deformation, attenuated creep, steady-state creep, and accelerated creep. High temperature significantly reduces the load-bearing capacity of red sandstone, especially when the temperature exceeds 200°C. Elevated temperature not only causes rock damage but also enhances its brittle response, manifested by a shortened duration of steady-state creep and an increased creep rate at the ultimate stress level.

3. A non-constant creep model, comprising a general Kelvin body and a fractional viscoplastic body, is proposed and successfully applied to describe experimental data of red sandstone under yield and failure stress levels. The model parameters are determined through numerical optimization, encompassing different deformation mechanisms of elasticity, viscoelasticity, and viscoplasticity. Sensitivity analysis highlights the significant impact of key parameters, such as shear modulus, viscosity coefficient, fractional order, and characteristic parameters, on the morphological aspects of red sandstone creep behaviour, emphasising the model's wide applicability in describing various creep patterns.

These conclusions provide essential insights into the mechanical properties of red sandstone in high-temperature environments, holding practical significance for applications in geological engineering, mining, and energy exploration.

References

[1] X. Jiang, X. Liang, Effects of In-Situ Mining of Oil Shale on Rock Mass Structure [J]. Journal of Northeastern University (Natural Science) **35** (3), 452 (2014). DOI: https://doi.org/10.3969/j.issn.1005-3026.2014.03.033

[2] E.T. Elliot, T.A. Buscheck, M. Celia, Active CO2 reservoir management for sustainable geothermal energy extraction and reduced leakage [J]. Greenhouse Gases: Science and Technology **3** (1), 50-65 (2013).
DOI: https://doi.org/10.1002/ghg.1328

[3]   S. Nagy, J. Siemek, Shale gas in Europe: the state of the technology-challenges and opportunities [J]. Archives of Mining Sciences **56** (4), 727-760 (2011).

[4]   S. Wang, S. Guo, Y. Yang, Complexity Study on Multi-Field Coupling Systems for Underground Coal Fires [J]. Sustainability **15** (17), 12918 (2023). DOI: https://doi.org/10.3390/su151712918

[5]   N. Slazak, D. Obracaj, M. Borowski, Methods for controlling temperature hazard in Polish coal mines [J]. Archives of Mining Sciences **53** (4), 497-510 (2008).

[6]   J. Wang, Deep geological disposal of high level radioactive waste in china:long-term plan and latest progress by 2004 [C]. The 13th International Conference on Nuclear Engineering (2004).

[7]   J.Y. Wang, F. Liu, Thermodynamic properties of soft sedimentary rock in geotechnical engineering [J]. Applied Mechanics and Materials **170**, 687-691 (2012).
      DOI: https://doi.org/10.4028/www.scientific.net/AMM.170-173.687

[8]   L. Deng, X. Li, Y. Wu, Influence of cooling speed on the physical and mechanical properties of granite in geothermal-related engineering [J]. Deep Underground Science and Engineering **1** (1), 40-57 (2022).
      DOI: https://doi.org/10.1002/dug2.12011

[9]   Y. Guo, L. Huang, X. Li, Experimental investigation on the effects of thermal treatment on the physical and mechanical properties of shale [J]. Journal of Natural Gas Science and Engineering **82**, 103496 (2020).
      DOI: https://doi.org/10.1016/j.jngse.2020.103496

[10] H. W. Zhou, T.L. Rong, L.J. Wang, A new anisotropic coal permeability model under the influence of stress, gas sorption and temperature: development and verification [J]. International Journal of Rock Mechanics and Mining Sciences **132**, 104407 (2020). DOI: https://doi.org/10.1016/j.ijrmms.2020.104407

[11] S. Liu, J. Xu, An experimental study on the physico-mechanical properties of two post-high-temperature rocks [J]. Engineering Geology **185**, 63-70 (2014). DOI: https://doi.org/10.1016/j.enggeo.2014.11.013

[12] H. Tian, T. Kempka, R. Schlüter, Influence of high temperature on rock mass surrounding in situ coal conversion sites [C]. 10th International Symposium on Environmental Geotechnology and Sustainable Development (2009).

[13] S.Q. Yang, B. Hu, Creep and long-term permeability of a red sandstone subjected to cyclic loading after thermal treatments [J]. Rock Mechanics and Rock Engineering **51**, 2981-3004 (2018).
      DOI: https://doi.org/10.1007/s00603-018-1528-8

[14] X. Pan, X. Zhou , Creep damage properties and nonlinear creep model of red sandstone treated at high temperature based on acoustic emission[J]. Acta Geotechnica, 1-19(2023).
      DOI: https://doi.org/10.1007/s11440-023-01832-5

[15] X. Ren, Y. Xin, B. Jia, Large Stress-Gradient Creep Tests and Model Establishment for Red Sandstone Treated at High Temperatures [J]. Energies **15** (20), 77-86 (2022). DOI: https://doi.org/10.3390/EN15207786

[16] X. Pan, F. Berto, X. Zhou, Creep mechanical characteristics and nonlinear viscoelastic-plastic creep model of sandstone after high temperature heat treatment [J]. Fatigue & Fracture of Engineering Materials & Structures **46** (8), 2982-3000 (2023). DOI: https://doi.org/10.1111/ffe.14061

[17] L. Chen, C.P. Wang, J.F. Liu, A damage-mechanism-based creep model considering temperature effect in granite [J]. Mechanics Research Communications **56**, 76-82 (2014). DOI: https://doi.org/10.1016/j.mechrescom.2013.11.009

[18] Y.L. Chen, J. Ni, W. Shao, Experimental study on the influence of temperature on the mechanical properties of granite under uniaxial compression and fatigue loading [J]. International Journal of Rock Mechanics and Mining Sciences **56**, 62-66 (2012). DOI: https://doi.org/10.1016/j.ijrmms.2012.07.026

[19] B. Zhang, C. Peng, S. Chen, The mechanical creep property of shale for different loads and temperatures [J]. International Journal of Rock Mechanics and Mining Sciences **163**, 105327 (2023).
      DOI: https://doi.org/10.1016/j.ijrmms.2023.105327

[20] E. Rybacki, G. Dresen, Creep behaviour of shale at elevated pressure and temperature conditions [C]. Fifth EAGE Shale Workshop. European Association of Geoscientists & Engineers (1), 1-3 (2016).

[21] C.B. Zhou, Z.J. Wan, Y. Zhang, Creep characteristics and constitutive model of gas coal under high-temperature triaxial stress [J]. Journal of Coal Science **37** (12), 2020-2025 (2012).
      DOI: https://doi.org/10.1007/s11783-011-0280-z

[22] S. Liu, Z. Huang, Investigations into Variations in Meso-and Macro-Physico mechanical Properties of Black Sandstone under High-Temperature Conditions Based on Nuclear Magnetic Resonance [J]. International Journal of Geomechanics **23** (3), 04022297 (2023). DOI: https://doi.org/10.1061/ijgnai.gmeng-7923

[23] Y. Wu, L.H. Hu, J. Yu, The sensitivity of mechanical properties and pore structures of Beishan granite to large variation of temperature in nuclear waste storage sites [J]. Environmental Science and Pollution Research **30**, 75195-75212 (2023). DOI: https://doi.org/10.1007/s11356-023-27510-3

[24] X. Pan, X. Zhou, Damage analysis of sandstone during the creep stage after high-temperature heat treatment based on NMR technology [J]. Rock Mechanics and Rock Engineering **55** (12), 7569-7586 (2022). DOI: https://doi.org/10.1007/S00603-022-03048-7

[25] M. Esmaili, S. R. Shadizadeh, B. Habibnia, Quantification of pore size distribution in reservoir rocks using MRI logging: A case study of South Pars Gas Field [J]. Applied radiation and Isotopes **130**, 172-187 (2017). DOI: https://doi.org/10.1016/j.apradiso.2017.09.033

[26] M. Kwaśniewski, Mechanical behaviour of rocks under true triaxial compression conditions – volumetric strain and dilatancy [J]. Archives of Mining Sciences **52** (3), 409-435 (2007).

[27] S. Traore, P.P. Naik, M. Mokhtari, Full-Field Creep Mapping in a Heterogeneous Shale Compared to a Sandstone [J]. Rock Mechanics and Rock Engineering **56** (1), 89-108 (2023). DOI: https://doi.org/10.1007/s00603-022-03073-6

[28] Ö. Aydan, T. Ito, U. Özbay, ISRM suggested methods for determining the creep characteristics of rock [J]. The ISRM Suggested Methods for Rock Characterization, Testing and Monitoring: 2007-2014, 115-130 (2015). DOI: https://doi.org/10.1007/978-3-319-07713-0_9

[29] H. Jia, S. Ding, Y. Wang, An NMR-based investigation of the pore water freezing process in sandstone [J]. Cold Regions Science and Technology **168**, 102893 (2019). DOI: https://doi.org/10.1016/j.coldregions.2019.102893

[30] H. Jia, F. Zi, G. Yang, Influence of pore water(ice) content on the strength and deformability of frozen argillaceous siltstone [J]. Rock Mechanics and Rock Engineering **53** (2), 967-974 (2020). DOI: https://doi.org/10.1007/s00603-019-01943-0

[31] X.P. Zhou, X.K. Pan, H. Cheng, The nonlinear creep behaviours of sandstone under the different confining pressures based on NMR technology [J]. Rock Mech. Rock Eng. **54**, 4889-4904 (2021). DOI: https://doi.org/10.1007/s00603-021-02557-1

[32] K. Shibata, K. Tani, T. Okada, Creep behaviour of tuffaceous rock at high temperature observed in unconfined compression test [J]. Soils and Foundations **47** (1), 1-10 (2007). DOI: https://doi.org/10.3208/sandf.47.1

[33] L.M. Gil-Martín, M.A. Fernández-Ruiz, E. Hernández-Montes, Mechanical characterization and creep behaviour of a stone heritage material used in Granada (Spain): Santa Pudia calcarenite [J]. Rock Mechanics and Rock Engineering **55** (9), 5659-5669 (2022). DOI: https://doi.org/10.1007/s00603-022-02946-0

[34] X. Yang, A. Jiang, X. Guo, Effects of water content and temperature on creep properties of frozen red sandstone: an experimental study [J]. Bulletin of Engineering Geology and the Environment **81** (1), 51 (2022). DOI: https://doi.org/10.1007/s10064-021-02553-3

[35] E.S Zha, Z.T. Zhang, R. Zhang, S.Y. Wu, C.B. Li, L. Ren, M.Z. Gao, J.F. Zhou, Long-term mechanical and acoustic emission characteristics of creep in deeply buried jinping marble considering excavation disturbance [J]. International Journal of Rock Mechanics and Mining Sciences **139** (1), 569-574 (2021). DOI: https://doi.org/10.1016/J.IJRMMS.2020.104603

[36] A. Serra-Aguila, J.M. Puigoriol-Forcada, G. Reyes, Viscoelastic models revisited: characteristics and interconversion formulas for generalised Kelvin-Voigt and Maxwell models [J]. Acta Mechanica Sinica **35**, 1191-1209 (2019). DOI: https://doi.org/10.1007/s10409-019-00895-6

[37] T.C. Kamdem, K.G. Richard, T. Béda, New description of the mechanical creep response of rocks by fractional derivative theory [J]. Applied Mathematical Modelling **116**, 624-635 (2023). DOI: https://doi.org/10.1016/j.apm.2022.11.036

[38] M. Li, J. Zhang, G. Meng, Testing and modelling creep compression of waste rocks for backfill with different lithologies [J]. International Journal of Rock Mechanics and Mining Sciences **125**, 104170 (2020). DOI: https://doi.org/10.1016/j.ijrmms.2019.104170